

GT2011-46+\$'

## MEASUREMENTS OF ADIABATIC FILM AND OVERALL COOLING EFFECTIVENESS ON A TURBINE VANE PRESSURE SIDE WITH A TRENCH

Jason E. Albert and David G. Bogard  
 University of Texas at Austin  
 Austin, Texas, USA

### ABSTRACT

Film cooling performance is typically quantified by separating the external convective heat transfer from the other components of the conjugate heat transfer that occurs in turbine airfoils. However, it is also valuable to assess the conjugate heat transfer in terms of the overall cooling effectiveness, which is a parameter of importance to airfoil designers. In the current study, adiabatic film effectiveness and overall cooling effectiveness values were measured for the pressure side of a simplified turbine vane model with three rows of showerhead cooling at the leading edge and one row of body film cooling holes on the pressure side. This was done by utilizing two geometrically identical models made from different materials. Adiabatic film effectiveness was measured using a very low thermal conductivity material, and the overall cooling effectiveness was measured using a material with a higher thermal conductivity selected such that the Biot number of the model matched that of a turbine vane at engine conditions. The theoretical basis for this matched-Biot number modeling technique is discussed in some detail. Additionally, two designs of pressure side body film cooling holes were considered in this study: a standard design of straight, cylindrical holes and an advanced design of “trenched” cooling holes in which the hole exits were situated in a recessed, transverse trench. This study was performed using engine representative flow conditions, including a coolant-to-mainstream density ratio of  $DR = 1.4$  and a mainstream turbulence intensity of  $Tu = 20\%$ .

The results of this study show that adiabatic film and overall cooling effectiveness increase with blowing ratio for the showerhead and pressure side trenched holes. Performance decreases with blowing ratio for the standard holes due to coolant jet separation from the surface. Both body film designs

have similar performance at a lower blowing ratio when the standard hole coolant jets remain attached. Far downstream of the cooling holes both designs perform similarly because film effectiveness decays more rapidly for the trenched holes.

### NOMENCLATURE

$Bi$	Biot number, $(h_f t_{wall})/k_{wall}$
$C$	airfoil chord length (linear distance from stagnation point to tail point)
$d$	cooling hole diameter
$DR$	coolant-to-mainstream density ratio, $\rho_c/\rho_\infty$
$h$	convective heat transfer coefficient
$H$	trench depth
$k$	thermal conductivity
$M$	blowing (mass flux) ratio, $\rho_c U_c / (\rho_\infty U_\infty)_{local}$
$M^*$	showerhead blowing (mass flux) ratio, $\rho_c U_c / (\rho_\infty U_\infty)_{approach}$
$Pr$	Prandtl number
$PS$	pressure (concave) side of airfoil
$Re$	Reynolds number
$s$	streamwise distance along model surface
$SS$	suction (convex) side of airfoil
$t$	thickness
$T$	temperature
$Tu$	turbulence intensity
$U$	velocity
$z$	spanwise distance along model surface

### Greek:

$\alpha$	cooling hole surface angle
$\beta$	cooling hole compound angle, relative to streamwise
$\delta$	uncertainty
$\eta$	adiabatic film effectiveness, $(T_\infty - T_{aw})/(T_\infty - T_c)$
$\phi$	overall cooling effectiveness at external surface of wall, $(T_\infty - T_{wall,ext})/(T_\infty - T_c)$
$\Lambda$	turbulence integral length scale
$\rho$	density

### Subscripts:

<i>aw</i>	adiabatic wall surface
<i>c</i>	coolant / gas at internal surface
<i>ext</i>	external surface
<i>f</i>	with film cooling / gas at external surface
<i>jet</i>	coolant jet temperature
<i>o</i>	without film cooling
<i>PS</i>	pressure side
<i>rec</i>	recovery temperature
<i>ref</i>	reference location
<i>Shd</i>	showerhead
<i>wall</i>	airfoil wall
$\infty$	local mainstream

### INTRODUCTION

The design of gas turbine airfoil film cooling configurations relies on experimental measurements to provide boundary condition data for analysis and to validate computational tools. A common technique for these experiments is to use low conductivity airfoil models to isolate the external and internal heat transfer effects, which allows for the direct measurement of the external convective boundary conditions associated with film cooling flows. These boundary conditions are usually nondimensionalized as adiabatic film effectiveness,  $\eta$  (defined below), and heat transfer coefficient augmentation ratio,  $h_f/h_o$ . These two parameters are used by engine designers to help calculate the resulting metal temperatures of an airfoil. The airfoil temperatures, which are of primary interest to engine designers, can be nondimensionalized as the overall cooling effectiveness,  $\phi$  (also defined below, in terms of the external wall temperature). When reporting experimental results in this paper,  $\eta$  is defined using the coolant jet temperature,  $T_{c,jet}$ , and  $\phi$  is defined using the coolant temperature at the reference location of the airfoil inlet,  $T_{c,ref}$ , which are standard conventions. In the following discussion about theory, a single coolant temperature is used in both  $\eta$  and  $\phi$  for simplicity, as shown in Eqns. 1 and 2. This generic coolant temperature,  $T_c$ , can be considered the internal coolant temperature at a particular location of the airfoil wall.

$$\eta = \frac{T_\infty - T_{aw}}{T_\infty - T_{c,jet}} \approx \frac{T_\infty - T_{aw}}{T_\infty - T_c} \quad (1)$$

$$\phi = \frac{T_\infty - T_{wall,ext}}{T_\infty - T_{c,ref}} \approx \frac{T_\infty - T_{wall,ext}}{T_\infty - T_c} \quad (2)$$

An alternate method of experimentally studying film cooling heat transfer is to use an airfoil model constructed from a material with a certain thermal conductivity so that the relative contributions of convection and conduction heat transfer are properly scaled. To do this the Biot number distribution of the airfoil is matched between the engine and experimental conditions. This approach also requires matching the external-to-internal heat transfer coefficient ratios ( $h_f/h_c$ ),

the adiabatic film effectiveness distribution ( $\eta$ ), and the scaled geometry between engine and experimental conditions. When all of this is done properly, the overall cooling effectiveness,  $\phi$ , measured on the model is the same as that of the corresponding airfoil at engine conditions. This “matched-Biot number” modeling technique is useful because it directly reveals how changes to internal and external heat transfer affect the metal temperature of the airfoil wall. Furthermore, it provides data that can be used to validate computational analyses of conjugate heat transfer.

The theoretical basis for the matched-*Bi* modeling technique can be demonstrated by performing a one-dimensional heat transfer analysis for an arbitrary location of a film-cooled airfoil wall, which results in Eqn. 3 when defining Biot number as  $Bi = (h_f t_{wall})/k_{wall}$ .

$$\phi = \frac{1 - \eta}{1 + Bi + \frac{h_f}{h_c}} + \eta \quad (3)$$

Equation 3 shows that when  $\eta$ ,  $Bi$ , and  $h_f/h_c$  (and, implicitly, the scaled geometry and flow fields) are matched between engine and experimental conditions, then  $\phi$  is also matched. This analysis defined the Biot number as a function of the full wall thickness,  $t_{wall}$ , and the external heat transfer coefficient,  $h_f$ . However, the conclusion would remain the same if some other definition of the Biot number were used (say, using half the wall thickness and the internal heat transfer coefficient,  $h_c$ ) as long as the Biot number was consistently defined for experimental and engine conditions. The values of every term of Eqn. 3 change for different locations on the airfoil, but the relation between them remains the same. The matched-*Bi* technique does not match a single value of Biot number, but it instead matches the distribution of Biot numbers throughout the portion of the airfoil being modeled.

In certain regions of an airfoil it is not adequate to assume one-dimensional heat transfer, such as near film cooling holes or internal walls. Nonetheless, the conclusion of Eqn. 3 remains valid for any three-dimensional region of an airfoil as long as the experimental conditions are properly established. Namely, if the geometry is properly scaled, the film effectiveness distribution is accurately modeled, the ratios of heat transfer coefficients between all convective surfaces are maintained, and the model’s thermal conductivity establishes the same Biot number (for any single location and definition of *Bi*), then the  $\phi$  distribution of the model will match that of the engine condition airfoil.

The current study utilizes a low-speed wind tunnel facility that does not attempt to match the Mach numbers of the engine conditions. For high-speed flows in engine conditions, convective heat transfer is driven by the recovery temperatures of the flows at the airfoil surfaces. In this case, Eqn. 3 remains valid as long as the definitions of  $\eta$  and  $\phi$  (Eqns. 1 and 2) use recovery temperatures for the gas flows (i.e.,  $T_{\infty,rec}$ ,  $T_{c,rec}$ , and

$T_{f,rec}$ ). This does not affect the measurements made with the experimental model, but it does affect how the measured  $\phi$  values should be interpreted for engine conditions.

The current study also utilizes much lower gas temperatures to model the airfoil heat transfer than exist in the engine conditions. As a result, the gas property variations for the engine conditions are not exactly simulated in the experimental model. The following discussion illustrates that this has a relatively small effect on the measured  $\phi$  values, which can be made even smaller by carefully designing the experimental conditions (e.g., by modifying the internal coolant flow Reynolds numbers). Consider one-dimensional heat transfer through a location of the airfoil wall, as described by Eqn. 3. The ratio of external-to-internal heat transfer coefficients can be expressed as a function of the Reynolds numbers, geometry, and fluid properties. This relation is shown in Eqn. 4 with  $C_1$ ,  $C_2$ ,  $a$ ,  $b$ ,  $m$ , and  $n$  being the appropriate constants for the Nusselt number correlations.

$$\frac{h_f}{h_c} = \frac{\left(\frac{Nu_x k}{x}\right)_f}{\left(\frac{Nu_{D_h} k}{D_h}\right)_c} = \frac{\left(\frac{C_1 Re_x^a Pr^b k}{x}\right)_f}{\left(\frac{C_2 Re_{D_h}^m Pr^n k}{D_h}\right)_c} \quad (4)$$

The matched- $Bi$  experimental technique requires that this heat transfer coefficient ratio should be the same for the model as it is in the engine conditions,  $(h_f/h_c)_{engine} / (h_f/h_c)_{model} = 1$ . This relation can be evaluated using Eqn. 4 for both engine and model conditions and then canceling out matched parameters, resulting in Eqn. 5. Proper design of the experimental facility will result in the parameters governing the geometry ( $D_h/x$ ) and the external flow field ( $C_1$  and  $Re_x$ ) to cancel out. Prandtl number changes negligibly between engine and experimental conditions, so it cancels out. Additionally, if the internal Reynolds number is matched, the internal flow parameters ( $C_2$  and  $Re_{D_h}$ ) cancel out. The resulting relation is as follows.

$$\frac{\left(\frac{h_f}{h_c}\right)_{engine}}{\left(\frac{h_f}{h_c}\right)_{model}} = \frac{\left(\frac{k_f}{k_c}\right)_{engine}}{\left(\frac{k_f}{k_c}\right)_{model}} \quad (5)$$

Gas thermal conductivities are practically insensitive to pressure, so Eqn. 5 is a function only of temperatures. Representative engine temperatures are  $T_f = 1681$  K (turbine inlet temperature) and  $T_c = 819$  K (compressor exit temperature) for an F100-PW-100 engine [1]. Representative experimental temperatures for the current study are  $T_f = T_\infty = 305$  K and  $T_c = 220$  K. Values of thermal conductivity for air at these temperatures yield  $(h_f/h_c)_{engine} / (h_f/h_c)_{model} = 1.39$ . The

effect of this mismatch on overall cooling effectiveness,  $\phi$ , can be determined with Eqn. 3. Using input values of  $\eta = 0$ ,  $Bi = 0.5$ , and  $(h_f/h_c)_{engine} = 0.5$ , this mismatch in  $h_f/h_c$  results in an overall cooling effectiveness error of  $\phi_{model} - \phi_{engine} = 0.04$ . Figure 1 shows how this error changes with  $\eta$  for constant values of  $Bi = 0.5$ , and  $(h_f/h_c)_{engine} = 0.5$ .

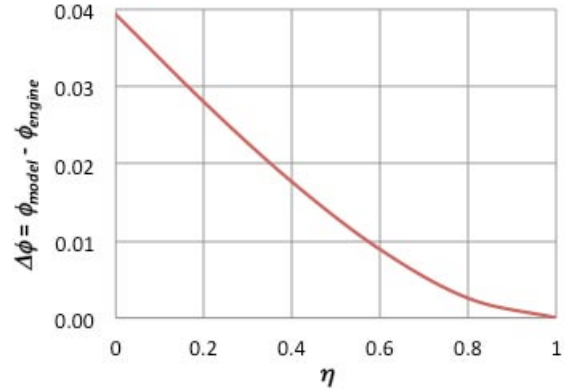


**Figure 1. Error in  $\phi$  caused by  $k_f/k_c$  discrepancy in matched- $Bi$  technique, for  $Bi=0.5$  and  $(h_f/h_c)_{engine}=0.5$**

Another way in which variable gas properties can affect the matched- $Bi$  experimental technique is by changing the relation between Nusselt number and Reynolds number for the flow over a surface. When there is a large temperature difference between the bulk of a gas and a surface, the fluid properties vary significantly near the surface. In this case the calculation of  $Nu$  should be modified as shown in Eqn. 6, where  $y$  is an empirical variable.

$$\frac{Nu}{Nu_{bulk}} = \left(\frac{T_{wall,ext}}{T_{bulk}}\right)^y \quad (6)$$

(Alternately, for external flows a mean film temperature can be used in lieu of Eqn. 6.) [2] This effect can change the ratio of heat transfer coefficients for a given location between the engine and experimental conditions, which will propagate to an error in  $\phi$ . Analysis shows that this error in  $\phi$  is about an order of magnitude less than the error caused by mismatching  $k_f/k_c$  (i.e., Eqn. 5) considering typical engine and experimental conditions.

Note that the errors relating to Eqns. 5 and 6 can be greatly reduced by adjusting the internal flow Reynolds number,  $Re_{D_h}$ , of the experimental model to set the desired magnitudes of  $h_c$ . This correction was not required in the current study because the experimental model was a generic design that did not simulate a specific engine condition.

The matched- $Bi$  experimental technique is a fairly recent development in turbine cooling research, and there are a limited number of studies in the literature that have utilized it. The first implementation of this technique was by Sweeney and Rhodes [3], who tested a large-scale model of a Lamilloy effusion-

cooled combustor lining that incorporated a double-walled arrangement with internal impingement cooling. The material conductivity of the model was selected to properly balance the convective and conductive heat transfer in the model so that it simulated the actual hardware in engine conditions.

Since then, this technique has been used several times by the laboratory at the University of Texas at Austin that produced the current study. Albert *et al.* [4] measured the adiabatic film and overall cooling effectiveness of a turbine blade leading edge model that was designed to match the Biot number of the corresponding engine hardware. Mouzon *et al.* [5] continued this work by measuring the heat transfer augmentation,  $h_f/h_o$ , of this model, which was combined with the  $\eta$  and  $\phi$  data to determine the net heat flux reduction provided by this film cooling arrangement. The matched-*Bi* leading edge model facility was also used in several other published studies since then. Dees *et al.* [6, 7] developed a matched-*Bi*, full airfoil model of a non-film-cooled turbine vane with an internal cooling arrangement consisting of a simple multi-pass serpentine channel arrangement. They measured the overall cooling effectiveness distribution on the vane external and internal surfaces and detailed measurements were made of the thermal and velocity profiles around the airfoil external surface. The experimental data was compared to computational results generated as part of those studies. The facility developed by Dees *et al.* has been utilized in the current study.

A film cooling design of interest to the current study is “trenched” film cooling, in which a row of straight, cylindrical cooling holes is situated in a transverse, recessed trench with a rectangular cross-section. Bunker [8] first published the concept of trenched film cooling, which included limited data regarding the increase in performance. This data was recorded using a flat plate wind tunnel facility. Trenched film cooling was experimentally studied in greater detail by Waye and Bogard [9], who found a significant enhancement of film cooling effectiveness for a trenched configuration compared to a comparable conventional design without a trench. This enhanced performance was attributed to the film coolant jets impinging on the downstream wall of the trench, spreading laterally within the trench, and forming a fairly continuous layer of film coolant (and high film effectiveness) downstream of the trench. Furthermore, Waye and Bogard tested various arrangements of trench edge shapes and trench widths for a constant trench depth of  $H/d = 0.5$ , and they determined that a rectangular cross section trench with a width of  $2d$  (equal to the length of the cooling hole footprint) was optimum for the nine geometries they tested. This work was performed on the suction side of a turbine vane airfoil model. Dorrington *et al.* [10] studied an expanded range of trench depths and widths, resulting in improved performance than that reported by Waye and Bogard. Their data showed that film effectiveness improved with trench depth, with most of the improvement occurring up to a depth of  $H/d = 0.75$ . They also found that performance was fairly insensitive to slight increases in trench width beyond the length of the cooling hole footprint. The

results of Dorrington *et al.* are the basis for selecting the trench geometry used in the current study.

The objective of the current study was to experimentally determine the adiabatic film effectiveness and overall cooling effectiveness of both standard and trenched film cooling holes on the pressure side of a turbine vane airfoil with showerhead film cooling. The adiabatic film effectiveness measurements utilized a low conductivity vane model, and the overall cooling effectiveness measurements were performed with a matched-*Bi* vane model with an identical geometry as the low conductivity model. This is the first published study of trenched film cooling on an airfoil pressure side and the first to measure overall cooling effectiveness for a trenched film cooling.

## EXPERIMENTAL FACILITIES AND PROCEDURES

All experiments for this study were performed in a closed-loop wind tunnel facility, shown schematically in Fig. 2. The wind tunnel mainstream flow was driven by 50 hp variable speed motor and fan, after which the flow passed through an arrangement of desiccant packs, a water-regulated heat exchanger, a series of honeycomb and screen partitions, and an area contraction before entering the test section. The test section incorporated a two-passage vane cascade with the full vane model in the middle being the test airfoil. A passive grid turbulence generator was situated at the entrance to the test section. It consisted of a row of vertical bars, 3.8 cm in diameter, with a centerline pitch of 8.9 cm, located 48.3 cm (0.938C) upstream of the vane nose point.

The external surface of the test vane was a 3.55 times scale geometry of the vane model used by Hylton *et al.* [11], which was in turn a 4.5 times scale model of a C3X vane design for the first stage nozzle of a helicopter engine [12]. The test vane of the current study was approximately 7 times larger than a typical commercial airplane engine first stage vane. The test vane had a chord length of  $C = 51.5$  cm (linear distance from stagnation point to tail point) and a span height of 54.8 cm. The pitch between stagnation lines of the vane passages was 45.7 cm. The stagnation line and pressure distribution for the test airfoil was adjusted using the flow bleeds at the sides of the test section and the adjustable outer wall of the suction side passage. Previous researchers in this facility measured the pressure distribution around the vane model and verified that it matched the design intent [6]. This measurement was performed once, and it was not repeated for each model installation. The test section was designed so that the test model could be easily and precisely replaced with a geometrically identical one, which allowed for different material conductivities to be tested in this study. The approximately adiabatic vane model was constructed from polyurethane foam with a conductivity of  $k = 0.048$  W/m·K. The matched-*Bi* model was constructed from Corian material, manufactured by DuPont, with  $k = 1.06$  W/m·K.

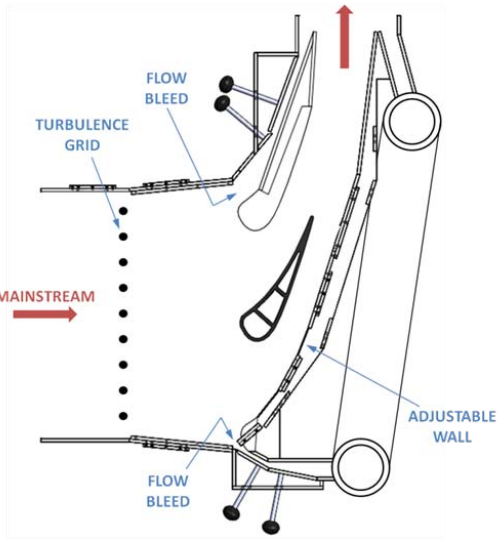
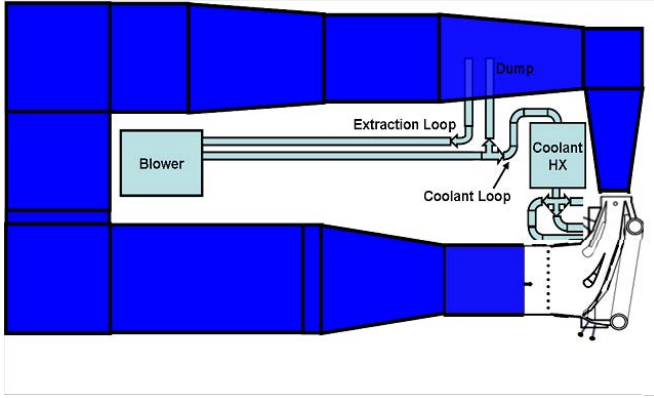


Figure 2. Wind tunnel and test section schematics

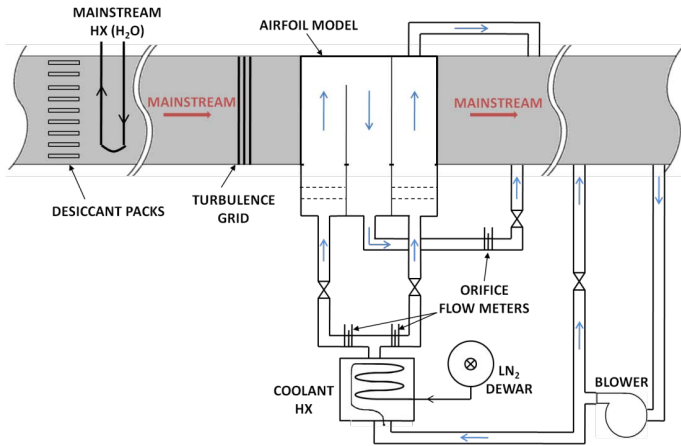


Figure 3. Coolant piping schematic

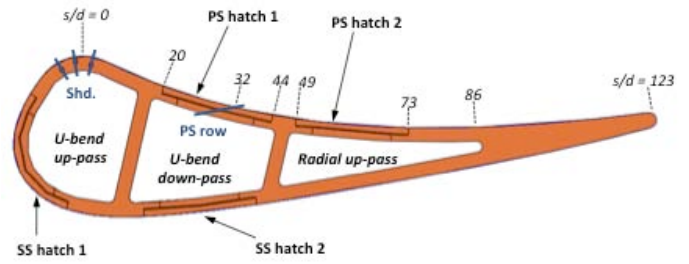


Figure 4. Vane model cross-section schematic with hatch locations shown

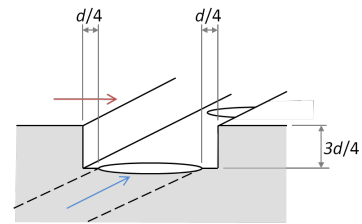


Figure 5. PS film row trenched cooling hole schematic

Corian material was selected for the matched- $Bi$  model in order to nominally match the distribution of Biot numbers for a turbine vane at engine conditions. The target Biot number range for this model was  $0.3 < Bi < 0.6$  to match engine conditions of a CFM56 high pressure turbine, based on input from collaborators at GE Global Research for a previous project in our laboratory [13]. The exact value of  $Bi$  will vary for different flow locations on an airfoil, depending on the mainstream flow field and how  $Bi$  is defined. Furthermore,  $Bi$  will vary between engine designs due to different combinations of  $t_{wall}$ ,  $h_f$ , and  $k_{wall}$  for a given location on an airfoil. For example,  $h_f$  can change  $\pm 30\%$  simply due to the range of turbine pressures typical of modern gas turbine engines (25-45 atm) relative to the CFM56 condition (32 atm), all other variables being equal. The matched- $Bi$  model in the current study was intended to be generally representative of high pressure turbine vane designs, and it was not meant to exactly simulate a specific design. Representative  $Bi$  values for the model used in this study are given in Table 1, with  $Bi$  defined as noted in the nomenclature.

A secondary flow loop powered by a 7.5 hp blower provided cooling air to the vane model. As shown in Fig. 3, the secondary flow was drawn from the tunnel mainstream by the blower, and then it passed it through a heat exchanger cooled by liquid nitrogen before splitting into the two dedicated cooling air circuits for the vane model. The vane cooling channels are shown in Fig. 4 – the “U-bend” coolant passage flowed up the forward internal channel, turned 180°, and then down the middle channel. The “radial” coolant passage flowed straight up the aft channel. Cooling air flow rates were controlled by two inlet valves in the secondary flow system upstream of the vane model, and additional control over the U-bend channel flow was provided by an outlet valve downstream

of the vane for that circuit. Orifice flow meters were used to measure the flow rates upstream of each control valve.

**Table 1. Representative  $Bi$  values for the matched- $Bi$  model**

	PS	SS
$k_{wall}$ (W/mK)	1.06	
$t_{wall}$ (mm)	13	
$h_f$ (W/m <sup>2</sup> K) [12]	40	70
$Bi$	0.5	0.9

**Table 2. Summary of experimental parameters**

Vane chord length, $C = 51.5$ cm	Cooling hole dia., $d = 4.22$ mm
Vane span height = 54.8 cm	<b>Showerhead:</b> surface angle, $\alpha = 25^\circ$ , compound angle, $\beta = 90^\circ$ , spanwise pitch, $p = 5.6d$ , length = $7.3d$
Mainstream velocity, $U_\infty = 5.8$ m/s	
Turbulence intensity, $Tu = 20\%$	<b>PS film:</b> surface angle, $\alpha = 30^\circ$ , compound angle, $\beta = 0^\circ$ , spanwise pitch, $p = 3.0d$ , length = $6.2d$ (without trench)
Turbulence integral length scale, $\Lambda = 3.7$ cm	
Mainstream exit $Re_c = 7.0 \times 10^5$	Coolant channels $Re_{Dh} = 2.0 \times 10^4$
Mainstream temp., $T_\infty = 305$ K	Coolant temp., $T_c = 220$ K Density ratio, $DR = 1.4$

Both versions of the vane model (low conductivity and matched- $Bi$ ) incorporated removable hatches on the pressure and suction sides, as shown in Fig. 4, that allowed for relatively quick changes in cooling hole configuration. For the current study, only the forward pressure side hatch was changed when switching between standard and trenched cooling holes. The other three hatches did not have any film cooling holes, and they remained unchanged for all experiments. The hatches were constructed of the same material as the vane model in which they were installed, and they were secured with small threaded connectors located outside the region of interest for measurements. The perimeters of the low conductivity polyurethane foam hatches were sealed with foam weather stripping and vacuum grease. The thermal discontinuities in the foam airfoil wall caused by the hatch perimeters did not affect the measurements of  $\eta$  because they were removed from the data using the conduction correction described later (Eqn. 7). The perimeters of the matched- $Bi$  Corian hatches were sealed with a non-hardening heat transfer compound. The thermal discontinuities in the Corian airfoil wall caused by the hatch perimeters had a minor local effect on the measured  $\phi$  values. The affected data points have been omitted from the laterally averaged  $\phi$  data, resulting in gaps about  $2d$ -long in the data sets at the hatch edge locations. In some data sets, the

thermal discontinuities caused slight changes in the slopes of the laterally averaged  $\phi$  data near the hatch perimeters.

All film cooling holes in the vane models had a diameter of  $d = 4.22$  mm. The vane model incorporated a three-row showerhead design, with one row biased towards the pressure side ( $s = 1.65d$ ) and two rows biased towards the suction side ( $s = 1.65d$  and  $4.95d$ ). The showerhead consisted of straight, cylindrical holes, all of which have a surface angle of  $\alpha = 25^\circ$ , a compound angle of  $\beta = 90^\circ$  with respect to the streamwise direction, and a centerline-to-centerline pitch of  $p = 5.6d$  in the spanwise direction. Each row was staggered a half-pitch in the spanwise direction from the adjacent row. A row of pressure side body film cooling holes was located at  $s = 32d$  from the stagnation line.

The “standard” design of body film holes consisted of straight, cylindrical holes that had a surface angle of  $\alpha = 30^\circ$ , a compound angle of  $\beta = 0^\circ$ , and a centerline-to-centerline pitch of  $p = 3d$  in the spanwise direction. The “trenched” design of body film holes was the same as the standard design except the hole exits were situated in a spanwise, recessed trench of rectangular cross-section, with dimensions as shown in Fig. 5. The trenched hole break-out location at the floor of the trench was exactly beneath the standard hole breakout location on the airfoil surface.

Experiments were performed using a mainstream temperature of  $T_\infty = 305$  K and a coolant temperature of about  $T_c = 220$  K to establish a coolant-to-mainstream density ratio of  $DR = 1.4$ . For all experiments, the mainstream approach velocity was  $U_{\infty, approach} = 5.8$  m/s, as measured by a Pitot-static probe, which corresponded with an exit velocity of 22 m/s at the vane trailing edge. The Reynolds number was  $Re_{C, exit} = 7.0 \times 10^5$ , when calculated using the airfoil chord length  $C$  and the exit velocity. The mainstream turbulence characteristics were measured across a plane 14.5 cm ( $0.282C$ ) upstream of the vane nose point, or 33.8 cm ( $0.656C$ ) downstream of the grid bars centerline. This yielded a turbulence intensity of  $Tu = 20\%$  and an integral length scale of  $\Lambda = 3.7$  cm ( $\Lambda/C = 0.072$ ). The coolant flow rates through the U-bend and radial channels were set to establish Reynolds numbers based on hydraulic diameters of nominally  $Re_{Dh} = 20,000$  for all blowing ratios. The total film cooling flow rate was determined by taking the difference between the measured inlet and exit coolant flow rates through the U-bend channel.

The film cooling flow split between the showerhead rows and the pressure side row was determined analytically as follows. The static pressure at the exit of each row of cooling holes was determined from a CFD study by Dees *et al.* [6], which has been verified to match the experimental model. Assuming a common supply pressure for the showerhead and pressure side cooling holes, the pressure ratio across each row of holes was found. The discharge coefficients for each row of holes were separately measured for a range of pressure ratios. When measuring these discharge coefficients, the mainstream and coolant flow Reynolds numbers were the same as a typical film cooling experiment, so the effects of internal and external

cross-flow were properly included. Combining the pressure ratios and discharge coefficients allowed for the fractional flow splits for each row of cooling holes to be calculated for a range of total film cooling flow rates. These fractional flow splits were multiplied by the measured total film cooling flow rate for each data point, yielding the flow rate for each row of holes and the resulting blowing ratios. The showerhead blowing ratio,  $M_{Shd}^*$ , was calculated considering all three rows combined, and it was a function of the mainstream approach velocity. The pressure side blowing ratio,  $M_{PS}$ , was calculated as a function of the local mainstream velocity at the hole exits.

The external surface temperatures of the model were measured using FLIR P20 and P25 infrared cameras, which viewed the model through NaCl salt crystal windows in the test section wall and ceiling. The IR cameras were calibrated *in situ* using thin-ribbon thermocouples mounted on the model surface at the coldest locations in the field of view (e.g., in film streaks) and just outside the region of interest for data processing. One or two calibration thermocouples were used per IR camera view. The model and thermocouples were painted flat black to establish a uniformly diffuse and high emissivity surface. The IR camera settings were held constant through all experiments. A calibration correlation for each camera was determined from the corresponding thermocouple measurements during the experiments. Calibration data were recorded for every experiment, and the IR camera calibrations were verified to remain essentially constant between experiments. The final calibration correlations were assembled from hundreds of data points over numerous experiments. The standard deviation of the thermocouple measurements relative to the calibration correlations was no more than  $\delta T_{wall,ext} = \delta T_{aw} = \pm 1.3$  K, which was the largest contributor to the uncertainty in effectiveness values  $\eta$  and  $\phi$ . Bias uncertainties for  $\eta$  and  $\phi$  were made negligible by calibrating the thermocouples used for  $T_c$  and  $T_\infty$  to those used for the IR camera calibrations.

A span covering five pressure side hole pitches at the model midspan was considered as the region of interest for effectiveness measurements. Almost the entire length of the vane pressure side could be measured simultaneously for each data point using the two infrared cameras. Post-processing the test data yielded adiabatic film effectiveness ( $\eta$ ) and overall cooling effectiveness ( $\phi$ ) of the region of interest, expressed in contour plots and laterally-averaged plots. For the adiabatic film effectiveness measurements, the small amount of conduction through the model wall was accounted for using the conduction correction formula shown as Eqn. 7. The parameter  $\eta_o$  was recorded with the internal flow active but the film cooling holes taped shut. Its typical range was  $0.03 < \eta_o < 0.11$ , and it varied only in the streamwise direction. This conduction correction technique was used by numerous previous researchers, and it can be derived using a one-dimensional heat transfer analysis of the airfoil model wall.

$$\eta = \frac{\eta_{measured} - \eta_o}{1 - \eta_o} \quad (7)$$

All uncertainties were calculated using the sequential perturbation method [14], and they are summarized here along with their most significant sources. The precision uncertainty for overall cooling effectiveness was  $\delta\phi = \pm 0.015$ . Because of the conduction correction, the adiabatic effectiveness had a higher uncertainty of  $\delta\eta = \pm 0.022$ . These uncertainties apply equally to both the local and laterally-averaged effectiveness measurements, and they were dominated by the IR camera calibration uncertainty noted above. Uncertainties for the blowing ratios were dominated by the measurements of the orifice meter pressure differentials,  $\delta(\Delta P_{inlet}) = \delta(\Delta P_{outlet}) = \pm 2.5$  Pa, and the film cooling hole discharge coefficients,  $\delta(C_d) = \pm 0.1$  (low  $M$ ) to  $\pm 0.01$  (high  $M$ ). The uncertainty in the blowing ratios was  $\delta M_{Shd}^* = \delta M_{PS} = \pm 0.25$ , which applies equally across low and high blowing ratios. The uncertainties of the mainstream flow conditions were  $\delta Tu = \pm 1.2\%$  (i.e.,  $\pm 6\%$  of the measured turbulence intensity of  $Tu = 19.9\%$ ),  $\delta A = \pm 0.85$  cm,  $\delta U_{\infty,approach} = \pm 0.08$  m/s, and  $\delta Re_{C,exit} = \pm 9,000$ . All uncertainties were consistent with numerous repeatability checks of data recorded at the same conditions in different experiments.

## RESULTS

Adiabatic film effectiveness ( $\eta$ ) was measured for the vane pressure side (PS) for a range of blowing ratios and two different film cooling configurations: showerhead + standard PS holes active and showerhead + trenched PS holes active. Before discussing these results, they are compared against similar data from the literature in Figs. 6 and 7.

Ames [12] reported measurements of adiabatic film effectiveness downstream of a row of holes ( $p/d = 3$ ,  $\alpha = 30^\circ$ ,  $\beta = 0^\circ$ ) on the pressure side of a C3X vane model. His data used the same airfoil and film cooling geometry as the current study, except his holes were located slightly further upstream on the pressure side and he did not have showerhead cooling holes. Furthermore, Ames' mainstream turbulence of  $Tu = 12\%$  was much less than that for the current study,  $Tu = 20\%$ , and he used a coolant density ratio of  $DR = 0.94$ , which was less than the density ratio of  $DR = 1.4$  used in this study. Despite these differences, the general trends of the adiabatic effectiveness distributions were very similar as shown in Fig. 6.

It is pertinent to also compare the film cooling performance measured for the trenched holes in the current study with other trenched hole data in the literature, although there are few other studies with similar geometry and conditions. Figure 7 compares data from the current study to data measured by Dorrington *et al.* [10]. There are differences in the geometry and flow conditions between Dorrington *et al.* and the current study, as noted in the legend of Fig. 7. The most significant difference is the much higher local turbulence of  $Tu = 17\%$  [13] at the PS trenched holes in the current study, as compared to  $Tu = 4\%$  at the SS trenched holes measured by Dorrington *et al.*

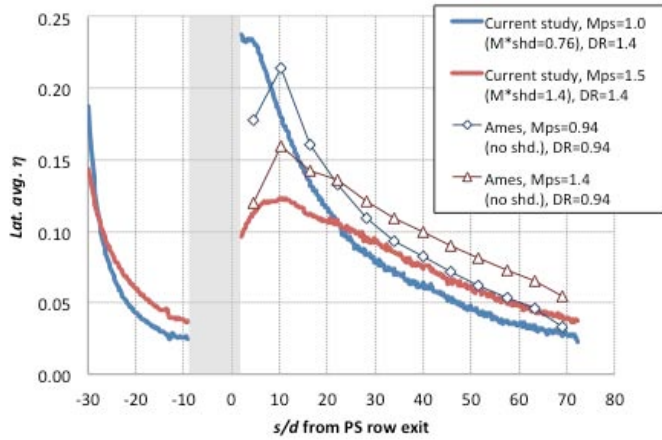


Figure 6. Comparison of adiabatic film effectiveness ( $\eta$ ) for standard PS holes to data from Ames [12]

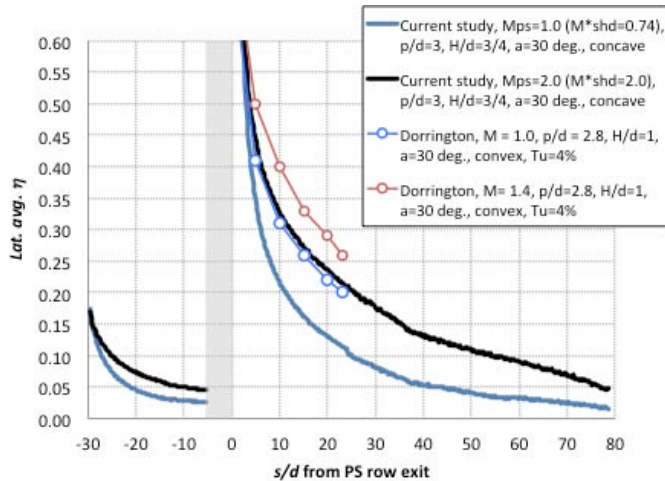


Figure 7. Comparison of adiabatic film effectiveness ( $\eta$ ) for trenced PS holes to data from Dorrington *et al.* [10]

The adiabatic film effectiveness measurements of the current study are presented in terms of their laterally averaged values in Figs. 8 and 9 as a function of streamwise surface distance ( $s/d$ ) from the stagnation line. Corresponding contour plots of  $\eta$  for the highest and lowest blowing ratios tested are presented in Figs. 10 and 11. It is obvious from these plots that the trenced holes had much higher  $\eta$  values than the standard holes just downstream of the PS row. However, the trenced hole film cooling decayed more rapidly than for the standard holes to the point where the  $\eta$  values were nominally equal between the two designs at about  $s/d = 100$  (Figs. 8 and 9). The reason for this difference in decay rate is speculated to be the thinner layer of film coolant established by the trenced holes, which mixed more rapidly with the mainstream than the standard holes case. Another plausible explanation for the rapid decay is that the film coolant from the trenced holes exited the trench at a lower velocity than the jets from the

standard holes, resulting in a stronger shear layer and more mixing with the mainstream flow.

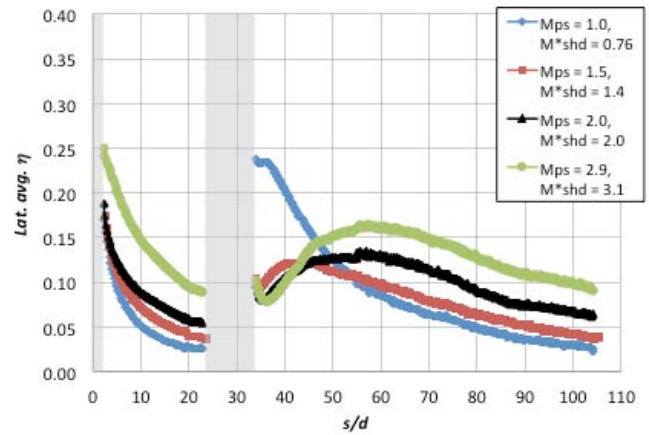


Figure 8. Showerhead + Standard PS holes laterally-averaged adiabatic film effectiveness ( $\eta$ ) for varying blowing ratios

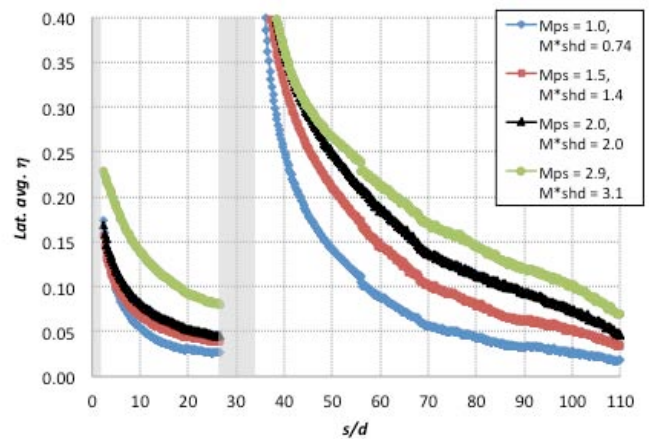
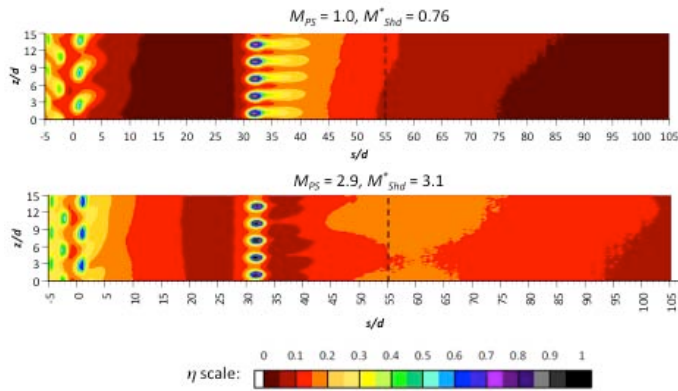
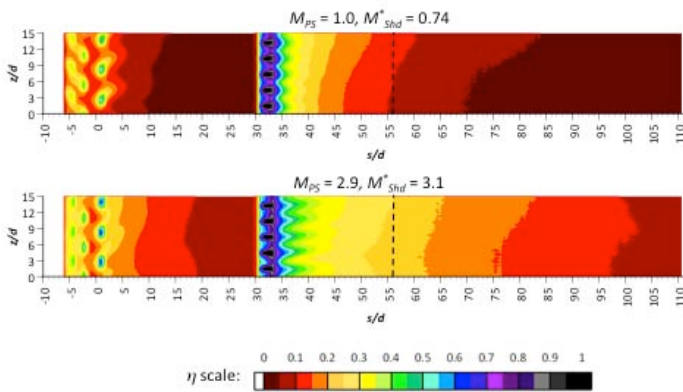


Figure 9. Showerhead + Trenced PS holes laterally-averaged adiabatic film effectiveness ( $\eta$ ) for varying blowing ratios

Another notable aspect in these data was the opposite trend of film effectiveness near the PS film row (i.e.  $s/d = 32$  to  $55$ ) with increasing blowing ratio for the standard versus trenced PS holes. The standard holes generated relatively high  $\eta$  for the lowest blowing ratio,  $M_{PS} = 1.0$ , for which the coolant jets were still partially attached to the airfoil surface (see Fig. 10). As the blowing ratio increased, the coolant jets detached from the surface, resulting in lower effectiveness values near the PS film row, as can be seen in Fig. 8. Conversely, the trenced holes performance increased near the PS film row as blowing ratio increased. This was because the trench arrangement prevented the coolant jets from fully separating from the airfoil surface, even at high blowing ratios (see Fig. 11).



**Figure 10. Showerhead + Standard PS holes adiabatic film effectiveness ( $\eta$ ) contours for low and high blowing ratios**



**Figure 11. Showerhead + Trenched PS holes adiabatic film effectiveness ( $\eta$ ) contours for low and high blowing ratios**

Figures 8 and 10 show evidence of coolant jet reattachment to the surface at the higher blowing ratios. Jet reattachment was most likely the cause of the higher  $\eta$  values at a location of about  $s/d = 50-60$ . It is uncommon to observe jet reattachment at a blowing ratio as high as  $M_{PS} = 3$ , and a likely reason for this is the concavity of the vane pressure side even though it was not highly curved. Pressure side film cooling jet reattachment at high blowing ratio is evident in the data presented by Ito *et al.* [15] for a more highly curved airfoil pressure side.

The  $\eta$  data downstream of the showerhead holes were nearly identical between the standard and trenched configurations. This was expected because these holes are geometrically identical for both models. This served as a confirmation of the repeatability of the showerhead blowing ratios for the different experiments. This was also an implicit confirmation of the cooling hole discharge coefficients used to calculate the film cooling flow splits for both configurations.

Overall cooling effectiveness ( $\phi$ ) was measured for the vane pressure side for a range of blowing ratios for both film cooling configurations. These data are presented in terms of their laterally-averaged values, as a function of streamwise

surface distance ( $s/d$ ) from the stagnation line, in Figs. 12 and 13. Corresponding contour plots of  $\eta$  for the highest and lowest blowing ratios tested are presented in Figs. 14 and 15.

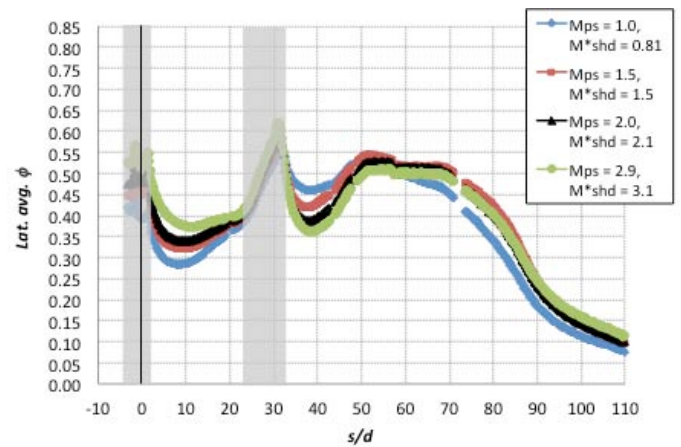


**Figure 12. Showerhead + Standard PS holes laterally-averaged overall cooling effectiveness ( $\phi$ ) for varying blowing ratios**

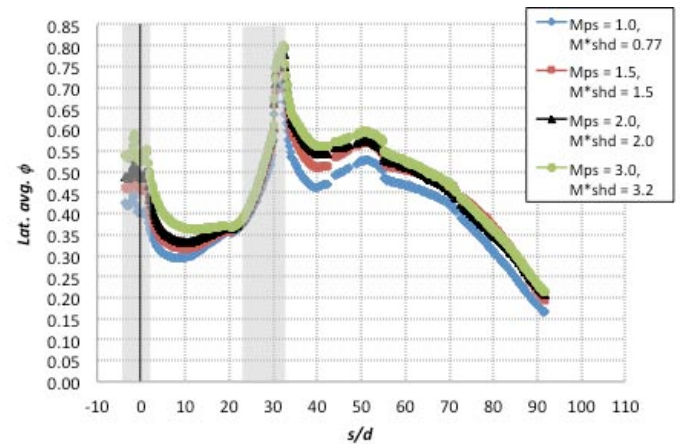


**Figure 13. Showerhead + Trenched PS holes laterally-averaged overall cooling effectiveness ( $\phi$ ) for varying blowing ratios**

As previously noted, the  $\eta$  values downstream of the PS holes had opposite trends with increasing blowing ratios for the standard and trenched holes due to coolant jet separation with the standard holes (see Figs. 8 and 9). This trend was also evident in the  $\phi$  data shown in Figs. 12 and 13, which was an illustration of how the adiabatic film effectiveness influences the overall cooling effectiveness. Another common aspect of the  $\eta$  and  $\phi$  data sets were the very similar values of  $\phi$  downstream of the showerhead holes in Figs. 12 and 13 ( $s/d = 0$  to 30), which was a confirmation of the repeatability of the blowing ratios and internal cooling flows between the matched-*Bi* model experiments using different PS film holes.

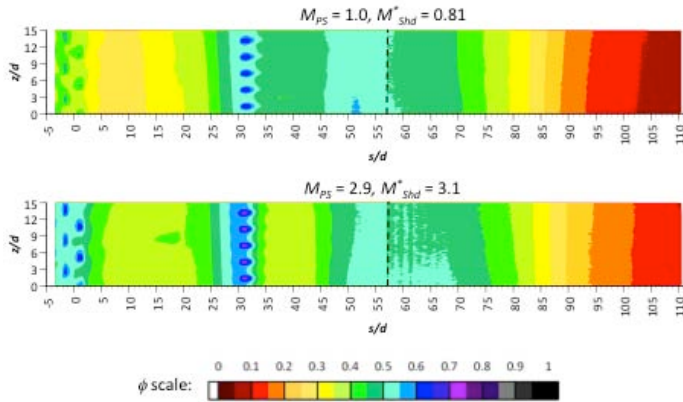


**Figure 14. Showerhead + Standard PS holes overall cooling effectiveness ( $\phi$ ) contours for low and high blowing ratios**

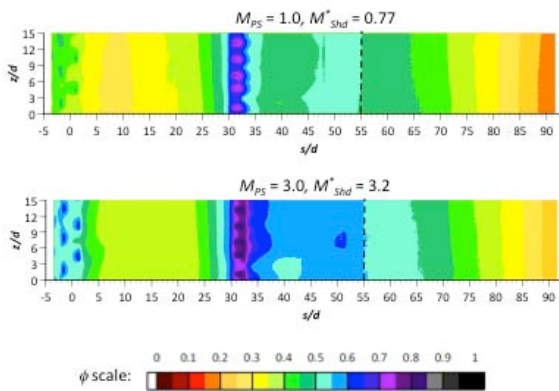


**Figure 15. Showerhead + Trenched PS holes overall cooling effectiveness ( $\phi$ ) contours for low and high blowing ratios**

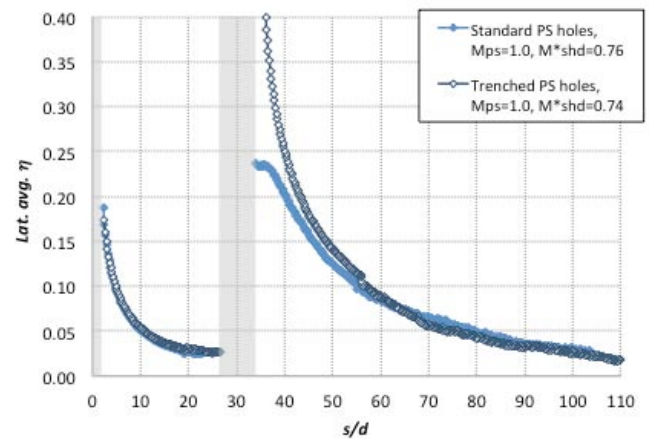
The rapid increase in  $\phi$  values just upstream of the PS film row ( $s/d = 23$  to  $32$ ) was caused by the convective cooling of the airfoil wall due to the PS film holes, which cooled the nearby external surface of the airfoil via conduction through the wall. As the angled cooling holes approached the external surface, the  $\phi$  value at the nearby external surface increased until a maximum was reached at the hole break-out location at  $s/d = 32$ . This effect was observed to a lesser extent in the  $\eta$  contour plots (see Fig. 10), but this region was omitted from the laterally averaged  $\eta$  data in Figs. 8 and 9 because the conduction correction could not account for conduction from active cooling holes.

The internal walls separating the cooling channels of the matched-*Bi* model acted as cooling fins or heat sinks to the external wall of the airfoil, and this effect was somewhat evident in the  $\phi$  data in Figs. 12 and 13. As shown in Fig. 4, the internal walls intersected the external PS wall at about  $s/d = 18$  and  $s/d = 47$ . This was a much weaker effect than the heat sink provided by the flow through the cooling holes because of the higher heat transfer coefficients in the cooling holes and

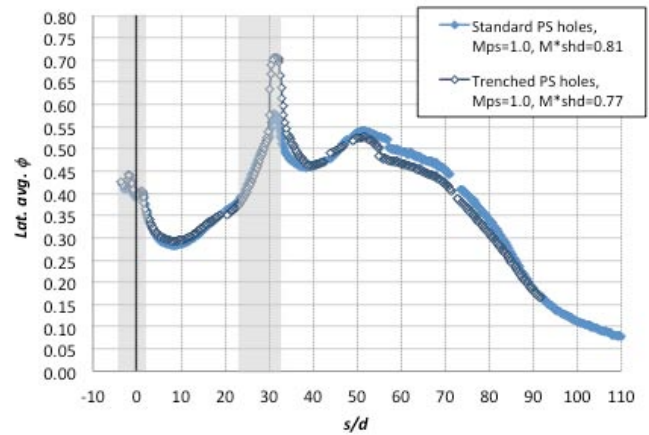
smaller conduction length scale between the cooling holes and airfoil external surface.

In order to better compare the performance of the standard and trenched PS holes, the lowest and highest blowing ratios from Figs. 8, 9, 12 and 13 are plotted in Figs. 16 and 17.

Figure 16 shows that the standard and trenched PS holes had nearly identical  $\phi$  performance at the lowest blowing ratio tested,  $M_{PS} = 1.0$ . This was due to the very similar  $\eta$  performance of the two designs at this blowing ratio. As discussed previously, the standard cooling hole jets remained mostly attached to the airfoil surface at this low blowing ratio, yielding higher  $\eta$  values that were similar to the trenched holes values.

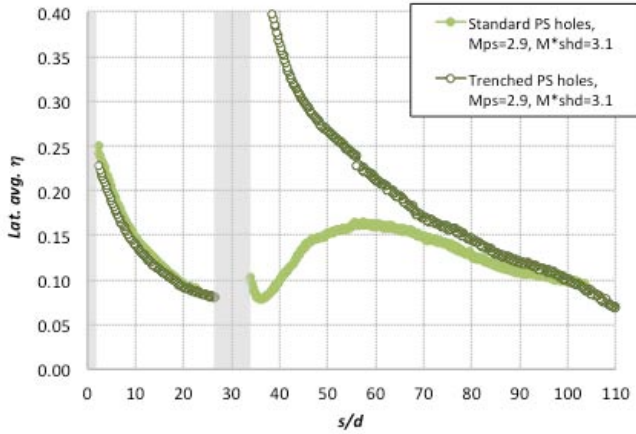


**(a) Adiabatic film effectiveness,  $\eta$**

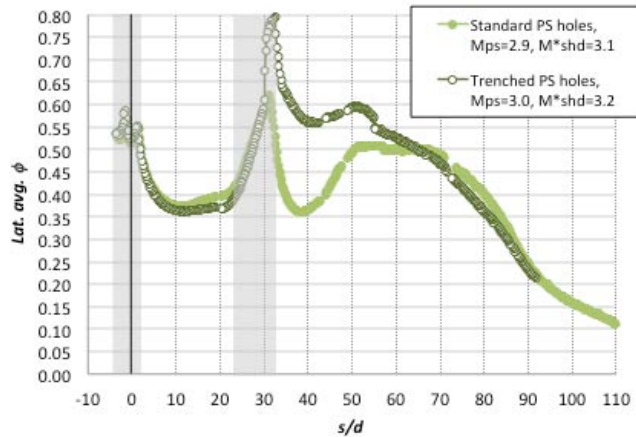


**(b) Overall cooling effectiveness,  $\phi$**

**Figure 16. Comparison of standard and trenched holes laterally-averaged  $\eta$  and  $\phi$  for lowest blowing ratio ( $M_{PS} = 1.0$ )**



(a) Adiabatic film effectiveness,  $\eta$



(b) Overall cooling effectiveness,  $\phi$

**Figure 17. Comparison of standard and trenched holes laterally-averaged  $\eta$  and  $\phi$  for highest blowing ratio ( $M_{PS} = 2.9-3.0$ )**

In Fig. 17 the trenched PS holes were clearly superior to the standard holes, in terms of  $\eta$  and  $\phi$ . This illustrated the benefit to the airfoil wall temperature when the coolant jets remained attached at a higher blowing ratio, as was the case for the trenched holes. Note that both designs had similar  $\eta$  and  $\phi$  values far downstream of the PS film row (about  $s/d > 70$ ), which was where the rapid decay of the trenched hole film cooling brought the  $\eta$  performance to a level much closer to the standard holes.

It is worthwhile to comment on the noticeably lower  $\phi$  values for the trenched holes compared to the standard holes in the range of about  $s/d = 55$  to  $80$  in Fig. 16(b), and to a lesser extent in Fig. 17(b). This seemed to be caused by a relatively large negative bias in the measured  $\phi$  data for the downstream infrared camera in the trenched hole  $\phi$  experiment. Nonetheless, both data sets in this range were within the uncertainty range that has been established for these measurements.

## CONCLUSIONS

Measurements of overall cooling effectiveness and adiabatic film effectiveness were performed on a turbine vane model with film cooling provided by a three-row showerhead and one row of pressure side holes. Two designs of pressure side holes were studied: a standard configuration of straight, cylindrical holes, and an advanced configuration of similar holes situated in a recessed, transverse trench. These measurements demonstrated the influence that film cooling performance has on the conjugate heat transfer in airfoil walls.

The trenched film hole configuration generally had much higher film effectiveness than the standard design just downstream of the holes because the trench prevents coolant jet separation from the airfoil surface. However, the trenched hole film coolant decays more rapidly than the standard hole design, resulting in nearly identical cooling of the airfoil wall further downstream from the holes.

The adiabatic film effectiveness just downstream of the cooling holes increased with blowing ratio for the trenched holes and decreased with blowing ratio for the standard holes. These opposite trends are due to the separation of the coolant jet from the airfoil surface, and these trends are also observed in the overall cooling effectiveness data. An exception to the superior performance of the trenched holes was observed at lower blowing ratios at which the standard hole coolant jets remain attached to the surface and provide similar cooling as the trenched holes. The opposing trends of film cooling performance with blowing ratio suggest that trenched film cooling holes are best suited for situations when the blowing ratio for a film row must be fairly high due to other airfoil cooling design constraints. Conversely, when the blowing ratio for a given film cooling row location can be fairly low, the added complexity of manufacturing trenched holes may not be beneficial.

The overall cooling effectiveness data illustrated the relative importance of internal cooling features on the airfoil external surface temperatures. For example, the convective cooling provided by flow through film cooling holes is dominant compared to the heat sink provided by the intersections of internal walls with the airfoil external wall.

Measurements of external and internal heat transfer coefficients,  $h_f$  and  $h_c$ , have not been performed in this study, so the measurements of  $\eta$  and  $\phi$  have not been compared against each other to further validate the matched- $Bi$  modeling technique. Equation 3 shows how this comparison would be done in a one-dimensional sense, which is primarily a conceptual aid. This comparison could also be done using a three-dimensional computational model by calculating the  $\phi$  distribution from the experimentally measured boundary conditions  $\eta$ ,  $h_f$ , and  $h_c$ . However, this would only validate the application of the boundary conditions to the conduction heat transfer simulation. A more meaningful use of the  $\eta$  and  $\phi$  data of the current study would be to compare them against the results of a full computational simulation of the flow field and conjugate heat transfer of this experimental facility. It is the hope of the authors that the current study will be useful in

validating computational models, in addition to the physical insight these experimental results provide.

## ACKNOWLEDGMENTS

This work was primarily supported by U. S. Department of Energy, National Energy Technology Laboratory (NETL) through the University Turbine Systems Research (UTSR) program, which has been coordinated by the South Carolina Institute for Energy Studies (SCIES) at Clemson University. Additional support was provided by the U. S. Department of Defense, Office of Naval Research (ONR) through the Electric Ship Research and Development Consortium (ESRDC).

The views expressed in this publication are those of the authors and do not reflect the official policy or position of the U. S. Government.

## REFERENCES

- [1] Mattingly, J.D., Heiser, W.H., and Pratt, D.T., 2002, Aircraft Engine Design, 2<sup>nd</sup> edition, American Institute of Aeronautics and Astronautics.
- [2] Kays, W.M., and Crawford, M.E., 1980, Convective Heat and Mass Transfer, 2<sup>nd</sup> edition, McGraw-Hill.
- [3] Sweeney, P.C., and Rhodes, J.F., 2000, "An Infrared Technique for Evaluating Turbine Airfoil Cooling Designs," *Journal of Turbomachinery*, Vol. 122, pp 170 – 177.
- [4] Albert, J.E., Bogard, D.G., and Cunha, F., 2004, "Adiabatic and Overall Effectiveness for a Film Cooled Blade," ASME Paper GT2004-53998.
- [5] Mouzon, B.D., Terrell, E.J., Albert, J.E., and Bogard, D.G., 2005, "Net Heat Flux Reduction and Overall Effectiveness for a Turbine Blade Leading Edge," ASME paper GT2005-69002.
- [6] Dees, J.E., Ledezma, G.A., Bogard, D.G., Laskowski, G.M., Tolpadi, A.K., 2010, "Experimental Measurements and Computational Predictions for an Internally Cooled Simulated Turbine Vane with 90 Degree Rib Turbulators," ASME paper GT2010-23004.
- [7] Dees, J.E., Ledezma, G.A., Bogard, D.G., Laskowski, G.M., Tolpadi, A.K., 2010, "Momentum and Thermal Boundary Layer Development on an Internally Cooled Turbine Vane," ASME paper GT2010-23008.
- [8] Bunker, R.S., 2002, "Film Cooling Effectiveness Due to Discrete Holes Within a Transverse Surface Slot," ASME Paper No. GT2002-30178.
- [9] Wayne, S.K., and Bogard, D.G., 2007, "High-resolution Film Cooling Effectiveness Measurements of Axial Holes Embedded in a Transverse Trench with Various Trench Configurations," *Journal of Turbomachinery*, Vol. 129, pp. 294-302.
- [10] Dorrington, J.R., Bogard, D.G., and Bunker, R.S., 2007, "Film Effectiveness Performance for Coolant Holes Embedded in Various Shallow Trench and Crater Depressions," ASME Paper No. GT2007-27992.
- [11] Hylton, L.D., Milhec, M.S., Turner, E.R., Nealy, D.A., and York, R.E., 1983, "Analytical and Experimental Evaluation of the Heat Transfer Distribution Over the Surface of Turbine Vanes," NASA CR 168015.
- [12] Ames, F.E., 1998, "Aspects of Vane Film Cooling with High Turbulence: Part II – Adiabatic Effectiveness," *Journal of Turbomachinery*, Vol. 120, pp. 777-784.
- [13] Dees, J.E., 2010, "Experimental Measurements of Conjugate Heat Transfer on a Scaled-up Gas Turbine Airfoil with Realistic Cooling Configuration," Ph.D. dissertation, The University of Texas at Austin.
- [14] Moffat, R.J., 1988, "Describing the Uncertainties in Experimental Results," *Experimental Thermal and Fluid Science*, Vol. 1, pp. 3-17.
- [15] Ito, S., Goldstein, R.J., Eckert, E.R.G., 1978, "Film Cooling of a Gas Turbine Blade," *Journal of Engineering for Power*, Vol. 100, pp. 476-481.